nature synthesis

Supplementary information

https://doi.org/10.1038/s44160-025-00914-4

Electrified vapour deposition at ultrahigh temperature and atmospheric pressure for nanomaterials synthesis

In the format provided by the authors and unedited

Table of Contents

Supplementary Note 1: Vapor flux calculations for EVD

We calculated the vapor flux of Ni atoms in the EVD process ($NiCl_2$ as precursor for simplicity) using Equation 1[1]:

$$F = \frac{p}{\sqrt{2\pi m k_B T}} \qquad (Eq\ 1)$$

Where F is the vapor flux, p is the partial pressure of the Ni vapor (~56200 Pa for EVD[2]), m is the mass of the Ni atom (9.74×10^{-26} kg), k_B is the Boltzmann constant (1.38×10^{-23} J/K), and T is the temperature of the vapor (1000–2000 K for EVD). Our results indicate that the flux of the vaporized species in EVD can reach 10^{21} –10^{22} atoms/cm^2/s.

Supplementary Note 2: Modeling the multi-elemental hexagonal $Mo_{45}Co_{25}Fe_{10}Ni_{10}Mn_{10}O_x$ nanodisks.

The elemental analysis results show $Mo_{45}Co_{25}Fe_{10}Ni_{10}Mn_{10}O_x$ has a hexagonal crystal structure following the $A_2B_3O_8$ formula, in which Mo primarily occupies the B sites, the Co and Ni predominately occupy the A sites, and the Mn and Fe appear to preside at both sites (Fig. 2c). Consequently, we constructed a multi-elemental oxide bulk crystal (Extended Data Fig. 6a), consisting of 9 Mo ions at the B sites, 5 Co ions at the A sites, 2 Ni ions at the A sites, 2 Mn ions at the B sites, one Fe ion at an A site and another Fe ion at a B site, and 32 O ions. The lattice parameter of the bulk crystal was predicted to be 5.87 Å, close to the experimentally observed 5.80 Å for the multi-elemental oxide (Extended Data Fig. 5a).

Supplementary Note 3: Oxidation energy calculation.

The adsorption energy of O on site X of multi-elemental hexagonal $Mo_{45}Co_{25}Fe_{10}Ni_{10}Mn_{10}O_x$ nanodisk surface (i.e., $E_{ad/X}$) was calculated as follow:

$$E_{ad/X} = E_{O/X} - E_{slab} - \mu_O$$

where $E_{O/X}$ is the system energy of O adsorbed on site X, E_{slab} is the energy of the clean surface, and μ_O is the chemical potential of O. Considering that O in multi-elemental oxides comes from oxygen molecule during synthesis, we assume that μ_O takes the value of half of μ_{O2}, which is the chemical potential of an oxygen gas molecule. Furthermore, μ_{O2} can be expressed as a function of temperature and pressure[3]:

$$\mu_{O2} = k_b T log\left(\frac{P\lambda^3}{k_b T}\right) - k_b T log\left(\frac{4\pi^2 I k_b T}{h^2}\right) + \frac{1}{2}\hbar\omega_0 + k_b T log[1 - exp\left(-\frac{\hbar\omega_0}{k_b T}\right)]$$

where T is temperature, P is pressure, k_b is the Boltzmann constant, h is the Planck's constant, and λ is the thermal de Broglie wavelength, I is the moment of inertia, and ω_0 is the vibrational frequency of the oxygen gas molecule O_2. The vibrational frequency of O_2 was calculated to be 1560.7 cm^{-1} using DFT, close to 1580.0 cm^{-1} measured in a previous study[4]. We set the temperature at 600 K and the pressure to be 10^{-5} atm in our calculations to be consistent with the experimental conditions.

In our model, there are multiple metal sites for O to be adsorbed on the multi-elemental oxide surface. Consequently, we calculated the adsorption energy of O at all possible metal sites on the exposed surface and further defined the surface oxidation energy to be the most negative adsorption energy among all possible values. Based on this definition, a more negative value of

the surface oxidation energy indicates a stronger attractive interaction between O and the corresponding oxide surface., i.e., a higher tendency for the surface to grow via oxidation.

Supplementary Note 4: The thermophoretic velocity calculation.

We estimated the thermophoretic velocity v_T of the vapor flow based on the established model [5,6], which we found can best resemble our EVD conditions.

$$v_T = -K_{th}\frac{\mu_g}{\rho_g}\frac{\nabla T}{T_g}$$

where ∇T is the temperature gradient close to the substrate, T_g the gas temperature, μ_g the dynamic viscosity of the argon gas, ρ_g the density of the argon gas, and K_{th} is the thermophoretic diffusion coefficient, which is calculated by the following equation:

$$K_{th,Beresnev} = \frac{\frac{6}{8+\pi}\left(\alpha_E + \frac{15}{8}\frac{\sqrt{\pi}(1-\alpha_E)}{\Lambda R}\right)\Phi_1 + \frac{\alpha_E \Phi_2}{\Lambda}}{\left(\alpha_E + \frac{15}{8}\frac{\sqrt{\pi}(1-\alpha_E)}{\Lambda R}\right)\Phi_3 + \left(\alpha_E + \frac{5}{8}\frac{\sqrt{\pi}(3-\alpha_E)}{\Lambda R}\right)\Phi_4}\left(\frac{F_3 + (1-\alpha_E)F_4}{F_1 + (1-\alpha_E)F_2}\right)$$

In the above equation, Λ is the ratio of thermal conductivity of argon gas to the nanomaterial, $\Phi_k = f_{k1} + (1-\alpha_T)f_{k2} + (1-\alpha_T)f_{k3}$, for $k = 1, 2, 3$ and 4, with α_E and α_T representing the energy and tangential momentum accommodation coefficients (in the case of complete accommodation, $\alpha_E = \alpha_T = 1$). $F_k = \phi_{k1} + (1-\alpha_T)\phi_{k2}$, for $k = 1, 2, 3$ and 4. $R = \sqrt{\pi}/(2Kn)$, where Kn is the Knudsen number defined as the ratio of the mean free path of argon atoms to the characteristic length (taken to be the radius of the particles formed). f_{ij} and φ_{ij} coefficients are tabulated in the original paper[5].

In this work, we used $NiCl_2$ as a representative precursor for demonstration purposes without loss of generality. We assume complete accommodation, i.e., $\alpha_E = \alpha_T = 1$, and we calculate the thermophoretic velocity. By 1) extrapolating the experimental data (e.g., gas temperature T_g (775K, extrapolated from Fig. 3c) and nucleated particle size (32.2 nm, extrapolated from Fig. 3f) and 2) looking up all the above coefficients based on the Kn number (calculated to be 37.2), we calculated the thermophoretic velocity to be ~0.0103 m/s ***towards*** *the substrate when the substrate temperature is 600 K, and ~0.0133 m/s* ***outwards*** *from the substrate when the substrate temperature is 1000 K. This estimation of thermophoretic velocity well explains what we observed in Fig. 3gii and 3hii, where nucleated particles in the EVD vapor do not deposit on the substrate when the substrate temperature is higher than that of the vapor, and vice versa.*

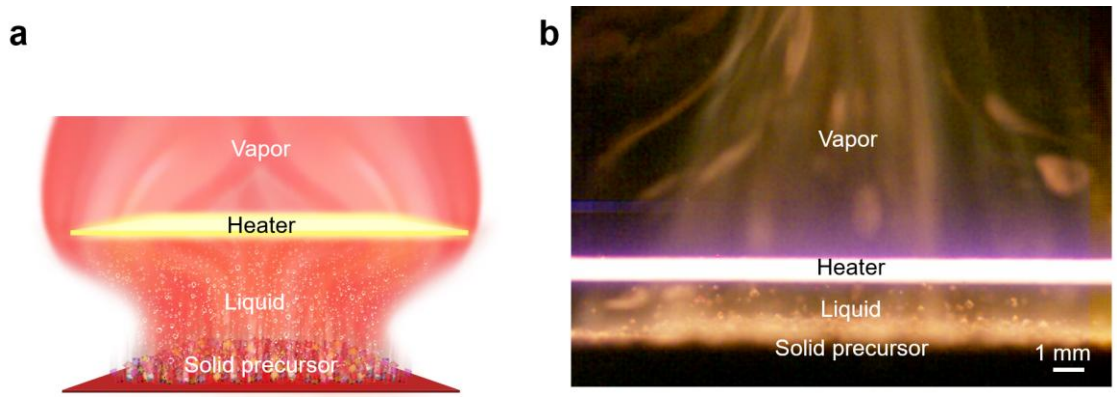

Supplementary Fig. 1. a, Schematic and **b**, digital image of the precursor during heating, captured using a high-speed camera (10000 frames/second). During imaging of the heating process, we found the solid-state precursor powders melt almost instantaneously into liquid spheres, which are rapidly evaporated into vapor within 5 ms.

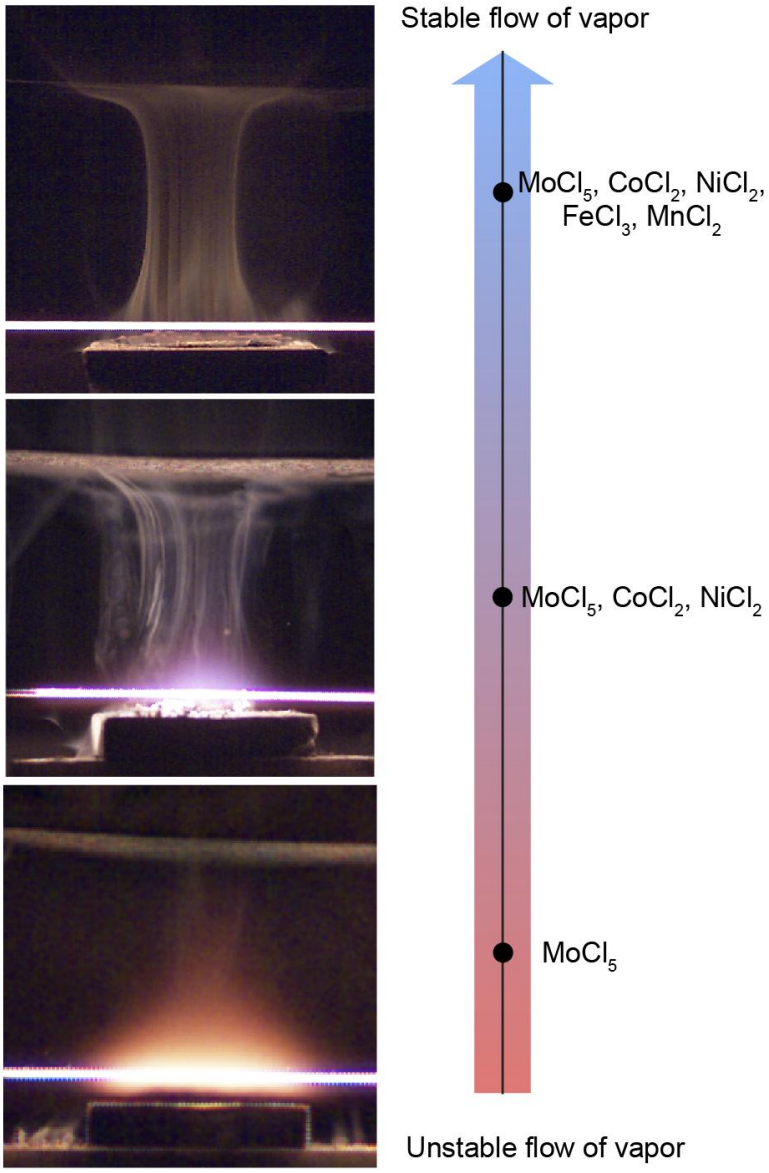

Supplementary Fig. 2. Digital images of the vapor flow for single ($MoCl_5$), ternary ($MoCl_5$, $CoCl_2$, $FeCl_2$, molar ratio = 45: 25: 10), and quinary precursor compositions ($MoCl_5$, $CoCl_2$, $FeCl_2$, $NiCl_2$, $MnCl_2$, molar ratio = 45: 25: 10: 10: 10) containing Mo. As a single species, Mo can barely evaporate due to its significantly lower vapor pressure[7]. However, it can be effectively vaporized when mixed with a higher ratio of easily evaporated metallic elements, which we believe may be due to interactions of Mo with more volatile species that help promote Mo into the vapor phase.

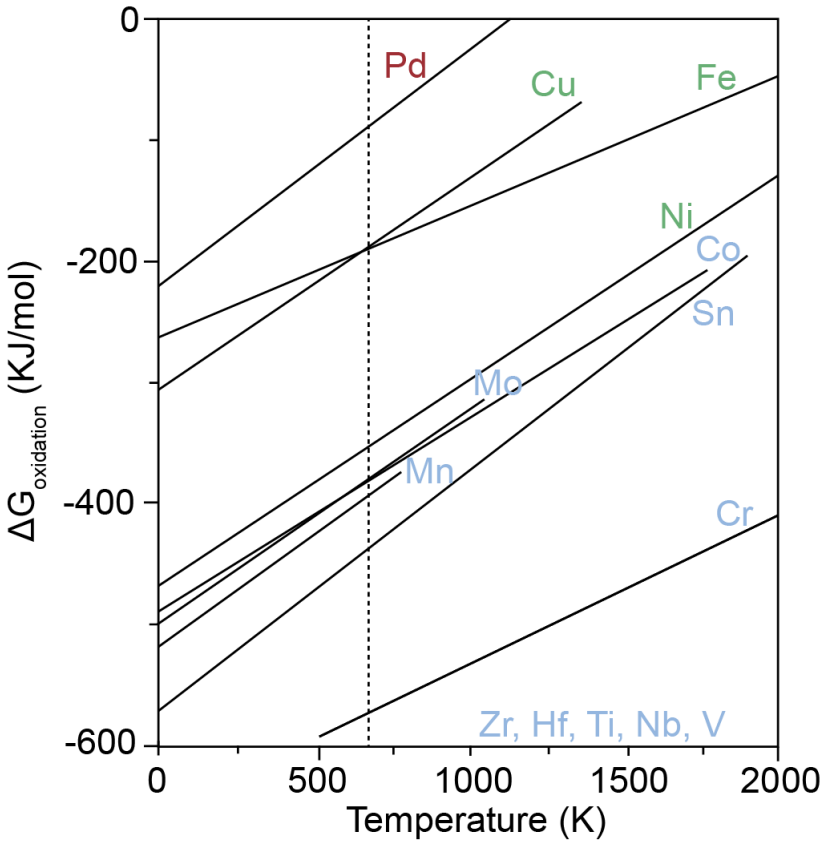

Supplementary Fig. 3. Ellingham diagram showing the elemental oxidation potentials (bulk materials, 1 atm partial pressure O2).[8,9] Easily oxidized elements are highlighted in blue, while red and green show less oxidized elements. At 600 K (average temperature of the substrate), a more negative $\Delta G_{oxidation}$ means easy oxidation to form oxide (e.g., Zr, Sn, Mo, Co, Mn, and Cr, marked in blue). As a result, we obtained ZrO_2 or SnO_2 thin films when using $ZrCl_4$ or $SnCl_2$ as precursors, and obtained $Mo_{45}Co_{25}Fe_yNi_yMn_{30-2y}O_x$ (y = 10, 12.5, and 15) when using $MoCl_5$ and $CoCl_2$-dominated precursors. A less negative $\Delta G_{oxidation}$ means tendency to form alloy (e.g., Pd marked in red). Elements in between (e.g., Cu, Fe, and Ni, marked in green) can form both alloy or oxide, depending on what oxidation behavior other elements demonstrate in the multi-elemental compositions. As a result, we obtained PdCuFeCoNi alloy as we have Pd elements which drive the formation of alloy.

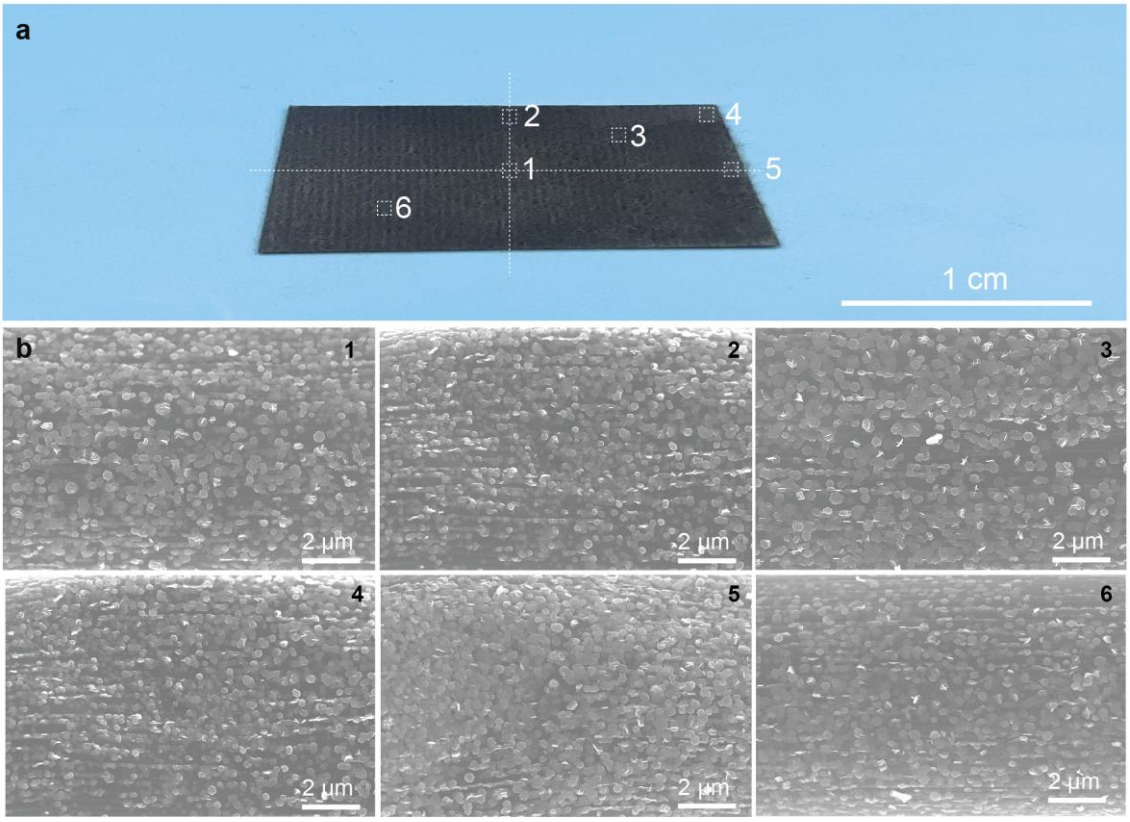

Supplementary Fig. 4. a, Photograph of the carbon paper substrate after EVD synthesis of the $Mo_{45}Co_{25}Fe_{10}Ni_{10}Mn_{10}O_x$ nanodisks. **b**, SEM images of the carbon paper substrate at six different locations, as noted in (A), demonstrating the uniform deposition of the nanodisks.

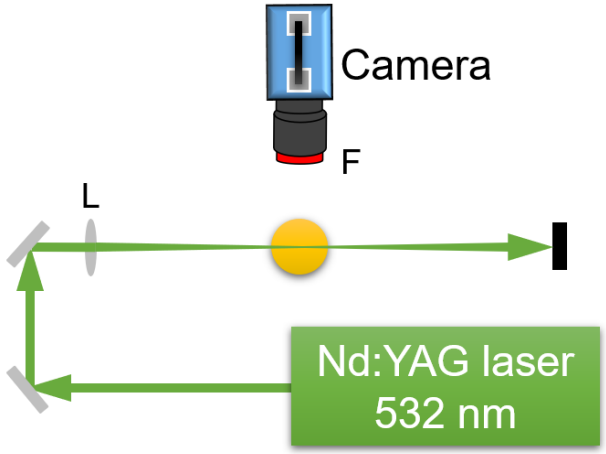

Supplementary Fig. 5 Schematic of LII. In the LII technique, a laser pulse heats any nanoparticles present in the gas phase to incandescent temperatures, causing them to produce LII signals.

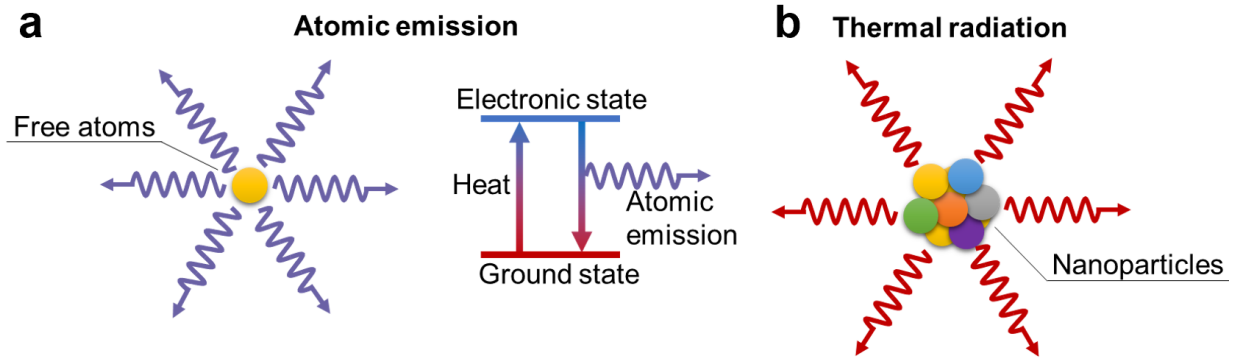

Supplementary Fig. 6 Schematics of **a,** atomic emission and **b,** thermal radiation from nanoparticles, produced during the EVD process. The emission of the "flame-like" appearance in the EVD process involves two components: (1) atomic emission from the electronically excited atoms in the vapor phase (Supplementary Fig. 6a), and (2) the thermal radiation of the nucleated nanoparticles due to the high temperature (Supplementary Fig. 6b).

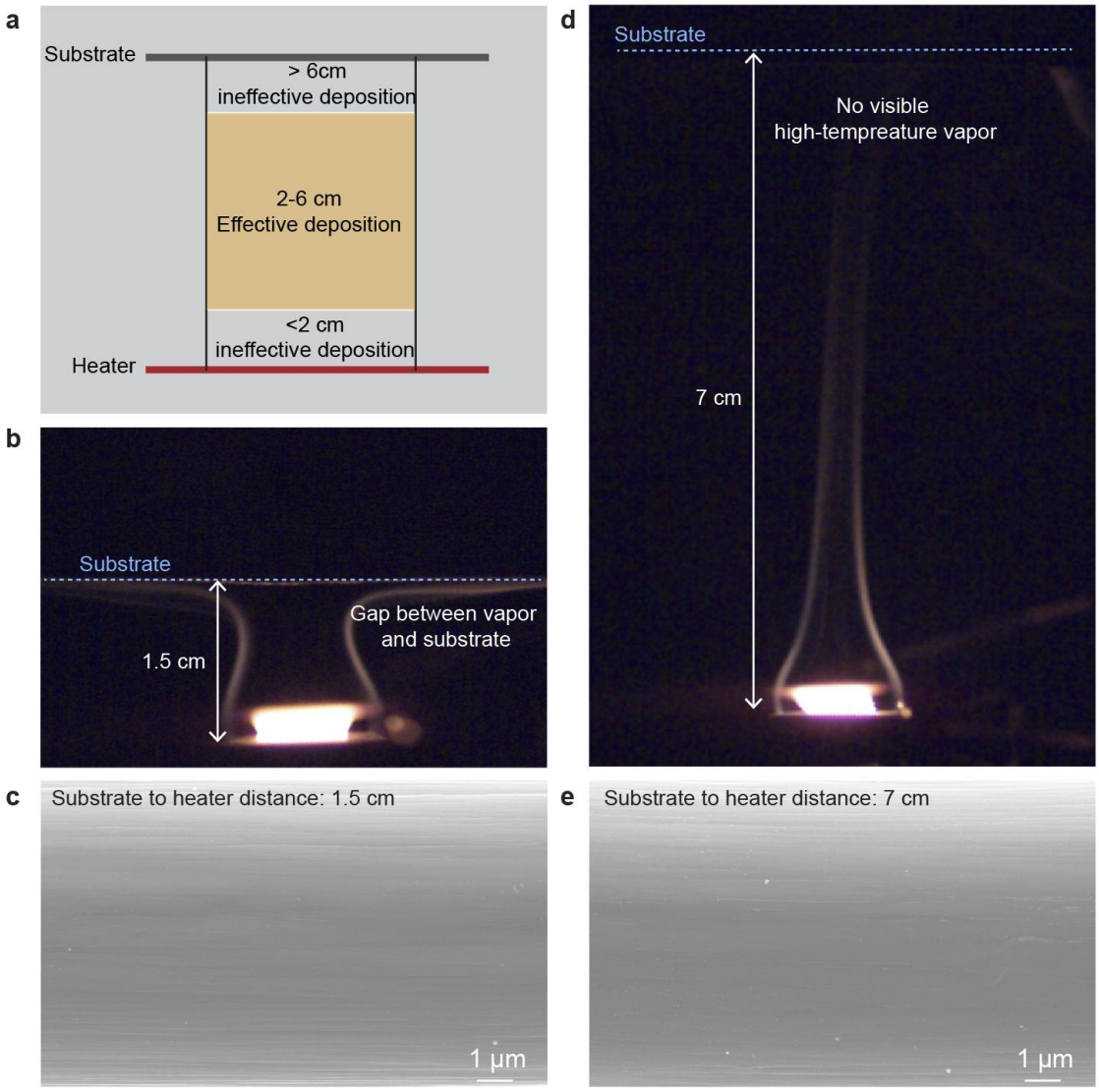

Supplementary Fig. 7. a, Schematic of the distance between the substrate and heater for effective deposition. **b**, Digital image showing the atomic vapor phase flowing around the substrate when the distance between the substrate and heater is ~1.5 cm. Under these conditions, the temperature of the substrate is too high (~2000 K after 0.3 s of heating), making it hard for the vapor phase species to nucleate on the hot substrate, in addition to the competing flow effects of the hot gas around the substrate, which limits the atomic vapor's contact with the surface. **c**, SEM image of the substrate when the distance between the substrate and heater is 1.5 cm, with no meaningful nanomaterials deposited, indicating ineffective deposition compared to Fig. 3giii. **d**, Digital image of the EVD process when the distance between the substrate and heater is 7 cm and **e**, a corresponding SEM image of the substrate, with no meaningful nanomaterials deposited. We conclude that there is a critical distance between the heater and substrate, which is above 2 cm and below 6 cm. Below this critical distance, the temperature of the substrate is too hot (~2000 K), which prevents effective product nucleation. However, above this critical distance, the particle deposition is also poor, which we hypothesize is due to the excessive growth of particles in the vapor phase, which may be too heavy to be collected effectively.

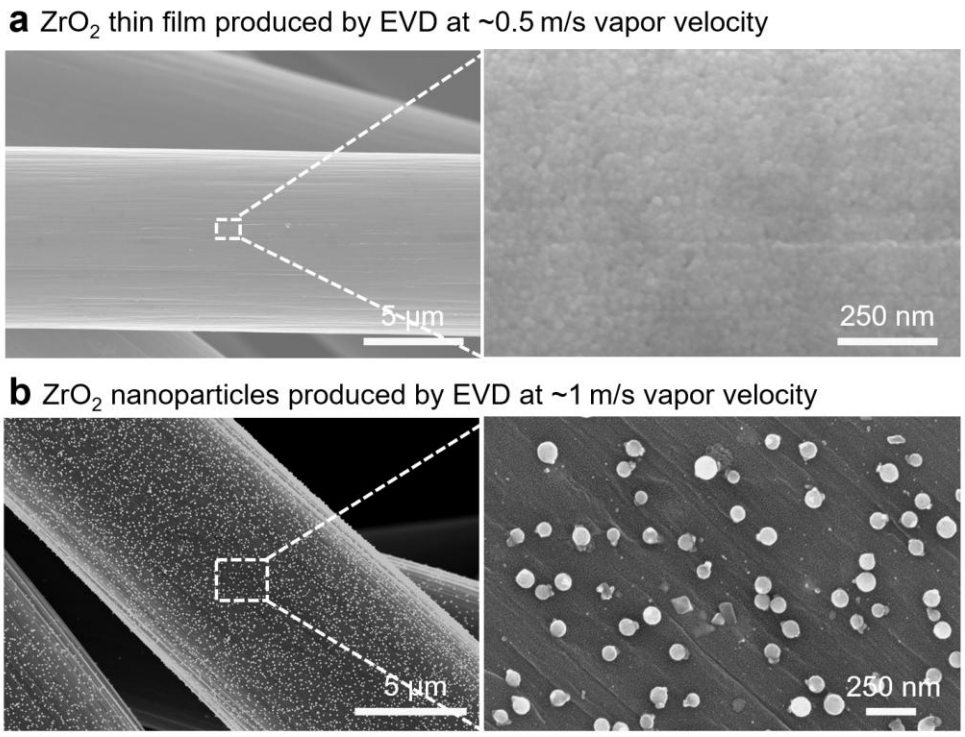

Supplementary Fig. 8 a, SEM images of ZrO_2 thin film produced by EVD at ~0.5 m/s vapor velocity. **b**, SEM images of ZrO_2 nanoparticles produced by EVD at ~1 m/s vapor velocity. We observed that ZrO_2 forms as a thin film at lower vapor velocities, whereas higher vapor velocities lead to the formation of nanoparticles, likely due to enhanced nucleation and growth rates under rapid vapor transport conditions.

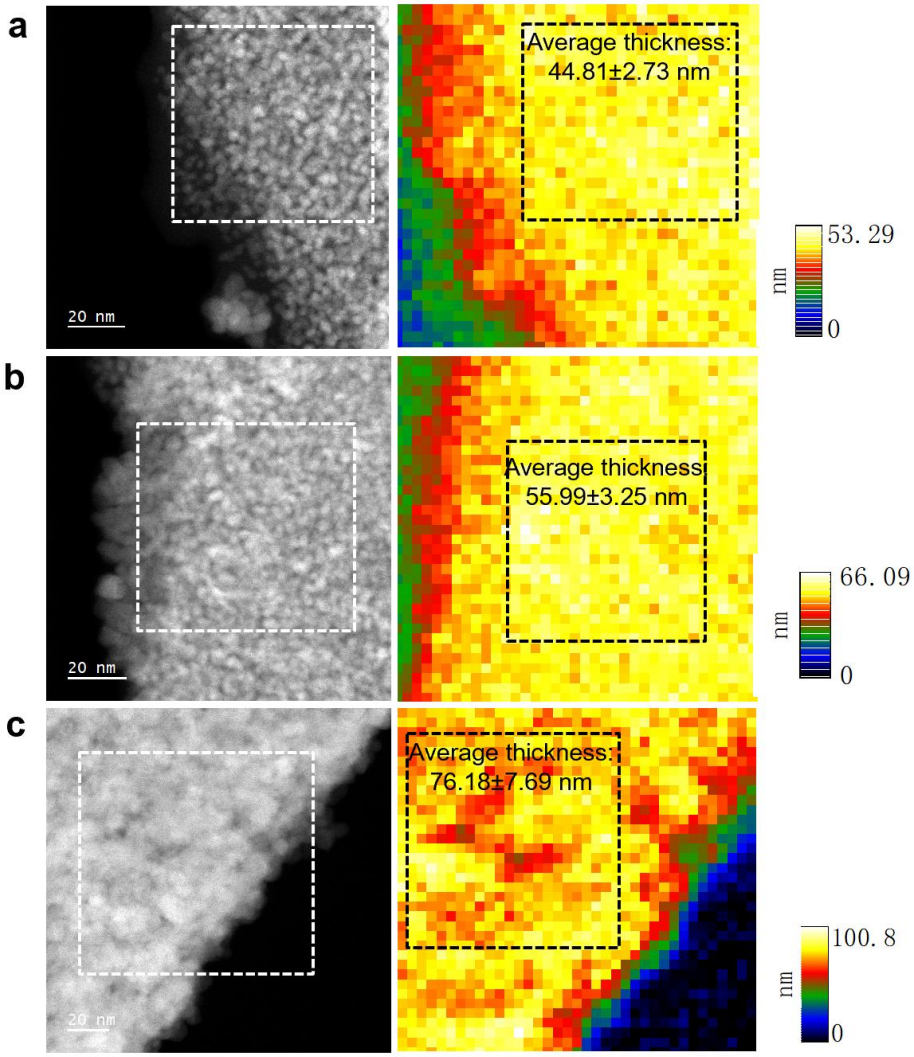

Supplementary Fig. 9 TEM images and thickness measurement of ZrO_2 film after **a** one, **b** two, and **c** three rounds of cycled heating (2 seconds, 4 seconds, 6 seconds of total deposition time, respectively) using $ZrCl_4$ as precursor.

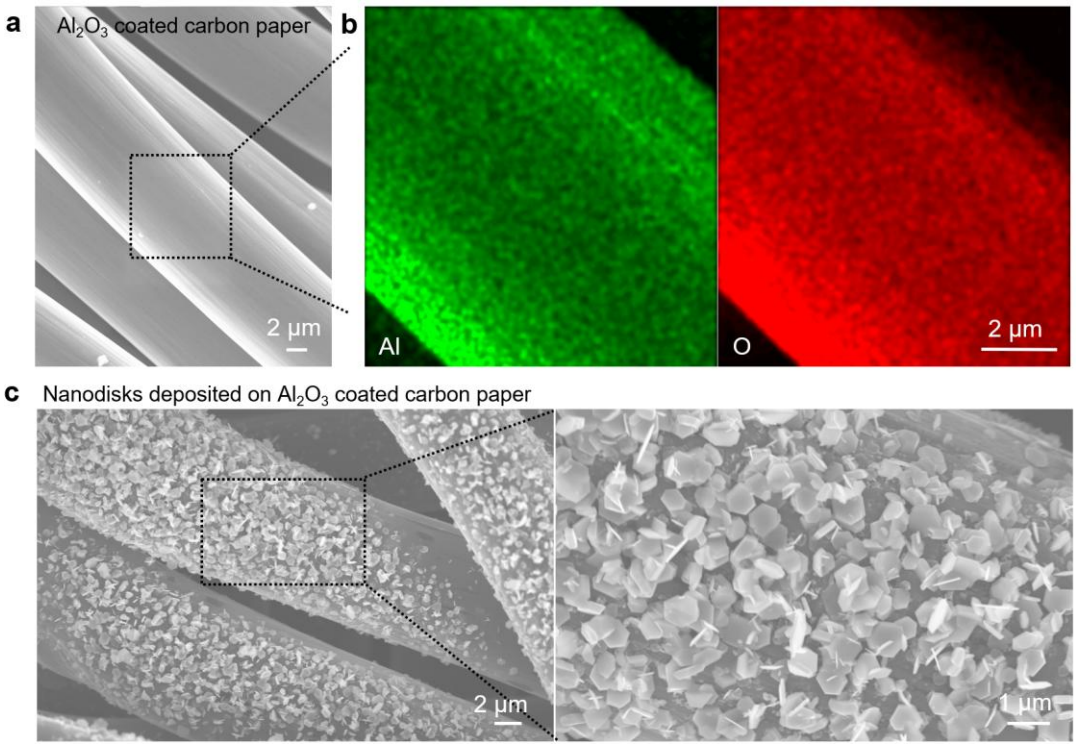

Supplementary Fig. 10 a, SEM and **b,** EDS images of Al_2O_3 coated carbon paper. **c,** SEM images of $Mo_{45}Co_{25}Fe_{10}Ni_{10}Mn_{10}O_x$ hexagonal nanodisks grown the Al_2O_3-coated carbon paper.

Supplementary Table 1. Comparison of EVD with common vapor-to-solid synthesis methods including thermal evaporation (TE), electron-beam evaporation (EBE), plasma enhanced chemical vapor deposition (PECVD), pulsed laser deposition (PLD), sputtering deposition (SD), and flame synthesis (FS).

	EVD	TE	EBE	PECVD	PLD	SD	FS
Vapor flux	10^{21}–10^{22} atoms/cm^2/s	10^{14}–10^{17} atoms/cm^2/s[10,11]	10^{13}–10^{17} atoms/cm^2/s[12,13]	10^{14}–10^{16} atoms/cm^2/s[14–16]	10^{13}–10^{16} atoms/cm^2/s[17–19]	10^{13}–10^{15} atoms/cm^2/s[20,21]	10^{19}~10^{21} atoms/cm^2/s[2,23]
Operating pressure	Atmospheric pressure	Requires low pressure (10^{-7}–10^{-5} Torr)[24,25]	Requires low pressure (typically 10^{-7}–10^{-4} Torr)[26,27]	Requires low pressure (typically 10^{-3}–10^{0} Torr)[28,29]	Requires low pressure (typically 10^{-8}–10^{-1} Torr)[30,31]	Requires low pressure (typically 10^{-6}–10^{-3} Torr)[32,33]	Atmospheric pressure[34]
Carrier gas	Not needed	Not needed	Not needed	Needed	Not needed	Not needed	Needed
Fuel	Not needed	Not needed	Not needed	Not needed	Not needed	Not needed	Needed
Oxidizer	Not needed	Not needed	Not needed	Not needed	Not needed	Not needed	Needed
Product	Complex alloys, oxides, sulfides, nanoparticles and thin films.	Typically thin films, single element metallic and conventional oxide nanoparticles, etc.[35–37]	Thin films, single or binary elements nanoparticles, etc.[38,39]	Thin films and single element metallic nanoparticles, etc.[22,40,41]	Thin film, single or binary element metallic nanoparticles, etc.[19,42,43]	Thin films and single element metallic nanoparticles, etc.[44,45]	Complex oxides and thin films[46,47]

Supplementary References:

1. Busuioc, S., Gibelli, L., Lockerby, D. A. & Sprittles, J. E. Velocity distribution function of spontaneously evaporating atoms. *Phys. Rev. Fluids* **5**, 103401 (2020).
2. Alcock, C. B., Itkin, V. P. & Horrigan, M. K. Vapour Pressure Equations for the Metallic Elements: 298–2500K. *Canadian Metallurgical Quarterly* **23**, 309–313 (1984).
3. Statistical Mechanics. *University Science Books* https://uscibooks.aip.org/books/statistical-mechanics/.
4. P, H. K. Constants of Diatomic molecules. *Molecular Spectra and molecular Structure* **4**, 146–291 (1979).
5. Beresnev, S. & Chernyak, V. Thermophoresis of a spherical particle in a rarefied gas: Numerical analysis based on the model kinetic equations. *Physics of Fluids* **7**, 1743–1756 (1995).
6. Sagot, B. Thermophoresis for spherical particles. *Journal of Aerosol Science* **65**, 10–20 (2013).
7. Alcock, C. B., Itkin, V. P. & Horrigan, M. K. Vapour Pressure Equations for the Metallic Elements: 298–2500K. *Canadian Metallurgical Quarterly* **23**, 309–313 (1984).
8. Chase, M. W., Jr. *et al.* JANAF Thermochemical Tables, 1982 Supplement. *Journal of Physical and Chemical Reference Data* **11**, 695–940 (1982).
9. Birks, N., Meier, G. H. & Pettit, F. S. *Introduction to the High Temperature Oxidation of Metals*. (Cambridge University Press, 2006).
10. Takamura, Y., Hayasaki, K., Terashima, K. & Yoshida, T. The role of radicals and clusters in thermal plasma flash evaporation processing. *Plasma Chem Plasma Process* **16**, S141–S156 (1995).
11. Tarkaeva, E. V., Ievleva, V. A., Duleba, A. I., Muratov, A. V. & Kuntsevich, A. Y. Amorphous VO$_x$ films with high temperature coefficient of the resistivity grown by reactive e-beam evaporation of V metal. Preprint at https://doi.org/10.48550/arXiv.2309.07036 (2023).
12. Dimoulas, A., Vellianitis, G., Travlos, A., Ioannou-Sougleridis, V. & Nassiopoulou, A. G. Structural and electrical quality of the high- *k* dielectric Y2O3 on Si (001): Dependence on growth parameters. *Journal of Applied Physics* **92**, 426–431 (2002).
13. Huynh, Q. T., Liu, C. Y., Chen, C. & Tu, K. N. Electromigration in eutectic SnPb solder lines. *Journal of Applied Physics* **89**, 4332–4335 (2001).
14. Bourdon, E. B. D., Raveh, A., Gujrathi, S. C. & Martinu, L. Etching of a-C:H films by an atomic oxygen beam. *Journal of Vacuum Science & Technology A* **11**, 2530–2535 (1993).
15. Komatsu, S., Kasamatsu, M., Yamada, K. & Moriyoshi, Y. Effects of plasma and/or 193 nm excimer laser irradiation on the surface in chemical vapor deposition of boron films from B2H6+He. *Applied Physics Letters* **59**, 608–610 (1991).
16. Czeremuszkin, G., Wertheimer, M. R., Cerny, J., Klemberg-Sapieha, J. E. & Martinu, L. Plasma-Deposited Coatings for the Protection of Spacecraft Materials Against Atomic Oxygen Erosion. in *Protection of Materials and Structures from the Low Earth Orbit Space Environment* (eds. Kleiman, J. I. & Tennyson, R. C.) 139–153 (Springer Netherlands, Dordrecht, 1999). doi:10.1007/978-94-011-4768-2_12.
17. Yang, W. *et al.* Epitaxial growth of single-domain graphene on hexagonal boron nitride. *Nature Mater* **12**, 792–797 (2013).
18. Beukers, J. N. *et al.* Epitaxial EuO thin films by pulsed laser deposition monitored by in situ x-ray photoelectron spectroscopy. *Thin Solid Films* **518**, 5173–5176 (2010).

19. Dikovska, A. O., Alexandrov, M. T., Atanasova, G. B., Tsankov, N. T. & Stefanov, P. K. Silver nanoparticles produced by PLD in vacuum: role of the laser wavelength used. *Appl. Phys. A* **113**, 83–88 (2013).
20. Thorsteinsson, E. B., Ingason, A. S. & Magnus, F. Magnetic ordering and magnetocrystalline anisotropy in epitaxial ${\mathrm{Mn}}_{2}\mathrm{GaC}$ MAX phase thin films. *Phys. Rev. Mater.* **7**, 034409 (2023).
21. Stilhano Vilas Boas, C. R., Sturm, J. M. & Bijkerk, F. Oxidation of metal thin films by atomic oxygen: A low energy ion scattering study. *Journal of Applied Physics* **126**, 155301 (2019).
22. Malekzadeh, M. & Swihart, M. T. Vapor-phase production of nanomaterials. *Chem. Soc. Rev.* **50**, 7132–7249 (2021).
23. Hunt, A. T., Carter, W. B. & Cochran, J. K., Jr. Combustion chemical vapor deposition: A novel thin-film deposition technique. *Applied Physics Letters* **63**, 266–268 (1993).
24. Umar, A., Kim, B.-K., Kim, J.-J. & Hahn, Y. B. Optical and electrical properties of ZnO nanowires grown on aluminium foil by non-catalytic thermal evaporation. *Nanotechnology* **18**, 175606 (2007).
25. Rabhi, A., Kanzari, M. & Rezig, B. Optical and structural properties of CuSbS2 thin films grown by thermal evaporation method. *Thin Solid Films* **517**, 2477–2480 (2009).
26. McMahon, S., Chaudhari, A., Zhao, Z. & Efstathiadis, H. Textured (111) crystalline silicon thin film growth on flexible glass by e-beam evaporation. *Materials Letters* **158**, 269–273 (2015).
27. Sahu, D. R., Wu, T.-J., Wang, S.-C. & Huang, J.-L. Electrochromic behavior of NiO film prepared by e-beam evaporation. *Journal of Science: Advanced Materials and Devices* **2**, 225–232 (2017).
28. Meyyappan, M., Delzeit, L., Cassell, A. & Hash, D. Carbon nanotube growth by PECVD: a review. *Plasma Sources Sci. Technol.* **12**, 205 (2003).
29. Gope, J., Kumar, S., Singh, S., Rauthan, C. M. S. & Srivastava, P. C. Growth of Mixed-Phase Amorphous and Ultra Nanocrystalline Silicon Thin Films in the Low Pressure Regime by a VHF PECVD Process. *Silicon* **4**, 127–135 (2012).
30. Rode, A. V., Luther-Davies, B. & Gamaly, E. G. Ultrafast ablation with high-pulse-rate lasers. Part II: Experiments on laser deposition of amorphous carbon films. *Journal of Applied Physics* **85**, 4222–4230 (1999).
31. Shepelin, N. A. *et al.* A practical guide to pulsed laser deposition. *Chem Soc Rev* **52**, 2294–2321.
32. Yang, S. *et al.* Influence of base pressure on property of sputtering deposited ITO film. *J Mater Sci: Mater Electron* **30**, 13005–13012 (2019).
33. Rossnagel, S. M. Magnetron sputtering. *Journal of Vacuum Science & Technology A* **38**, 060805 (2020).
34. Kammler, H. K., Mädler, L. & Pratsinis, S. E. Flame Synthesis of Nanoparticles. *Chemical Engineering & Technology* **24**, 583–596 (2001).
35. Gingery, D. & Bühlmann, P. Formation of gold nanoparticles on multiwalled carbon nanotubes by thermal evaporation. *Carbon* **46**, 1966–1972 (2008).
36. Gaspar, D. *et al.* Influence of the layer thickness in plasmonic gold nanoparticles produced by thermal evaporation. *Sci Rep* **3**, 1469 (2013).
37. Timoumi, A., Bouzouita, H., Kanzari, M. & Rezig, B. Fabrication and characterization of In2S3 thin films deposited by thermal evaporation technique. *Thin Solid Films* **480–481**, 124–128 (2005).

38. Nomoev, A. V. *et al.* Structure and mechanism of the formation of core–shell nanoparticles obtained through a one-step gas-phase synthesis by electron beam evaporation. *Beilstein J. Nanotechnol.* **6**, 874–880 (2015).
39. Zhang, X., Li, Y., Luo, X. & Ding, Y. Enhancing antibacterial property of porous titanium surfaces with silver nanoparticles coatings via electron-beam evaporation. *J Mater Sci: Mater Med* **33**, 57 (2022).
40. Lee, M. W., Haniff, M. A. S. M., Teh, A. S., Bien, D. C. S. & Chen, S. K. Effect of Co and Ni nanoparticles formation on carbon nanotubes growth via PECVD. *Journal of Experimental Nanoscience* **10**, 1232–1241 (2015).
41. Vasudev, M. C., Anderson, K. D., Bunning, T. J., Tsukruk, V. V. & Naik, R. R. Exploration of Plasma-Enhanced Chemical Vapor Deposition as a Method for Thin-Film Fabrication with Biological Applications. *ACS Appl. Mater. Interfaces* **5**, 3983–3994 (2013).
42. Dikovska, A. O. *et al.* Fabrication of Nanostructures Consisting of Composite Nanoparticles by Open-Air PLD. *Coatings* **14**, 527 (2024).
43. Singh, R. K. & Narayan, J. Pulsed-laser evaporation technique for deposition of thin films: Physics and theoretical model. *Phys. Rev. B* **41**, 8843–8859 (1990).
44. Wender, H., Migowski, P., Feil, A. F., Teixeira, S. R. & Dupont, J. Sputtering deposition of nanoparticles onto liquid substrates: Recent advances and future trends. *Coordination Chemistry Reviews* **257**, 2468–2483 (2013).
45. Mahne, N., Čekada, M. & Panjan, M. Total and Differential Sputtering Yields Explored by SRIM Simulations. *Coatings* **12**, 1541 (2022).
46. Liu, S. *et al.* A general flame aerosol route to high-entropy nanoceramics. *Matter* **7**, 3994–4013 (2024).
47. Hong, H., Xiong, G., Dong, Z., Kear, B. H. & Tse, S. D. Open-atmosphere flame synthesis of monolayer graphene. *Carbon* **182**, 307–315 (2021).